Influence of the Nanoscale Kirkendall Effect on the Morphology of Copper Indium Disulfide Nanoplatelets Synthesized by Ion Exchange

Linjia Mu, Fudong Wang, Bryce Sadtler, Richard A. Loomis, and William E. Buhro*

Department of Chemistry, Washington University, St. Louis, Missouri 63130-4899, United States

ABSTRACT $CuInS_2$ nanocrystals are prepared by ion exchange with template $Cu_{2-x}S$ nanoplatelets and InX_3 [X = chloride, iodide, acetate (OAc), or acetylacetonate (acac)]. The morphologies of the resultant nanocrystals depend on the InX_3 precursor and the reaction temperature. Exchange with $InCl_3$ at 150 °C produces $CuInS_2$ nanoplatelets having central holes and thickness variations, whereas the exchange at 200 °C produces intact $CuInS_2$ nanoplatelets in which the initial morphology is preserved. Exchange with InI_3 at 150 °C produces $CuInS_2$ nanoplatelets in which the central hollowing is more extreme, whereas exchange with $In(OAc)_3$ or $In(acac)_3$ at 150 °C produces intact $CuInS_2$ nanoplatelets. The results establish that the ion exchange occurs through the thin nanoplatelet edge facets. The hollowing and hole formation are due to a nanoscale Kirkendall Effect operating in the reaction-limited regime for displacement of X^- at the edges, to allow insertion of In^{3+} into the template nanoplatelets.

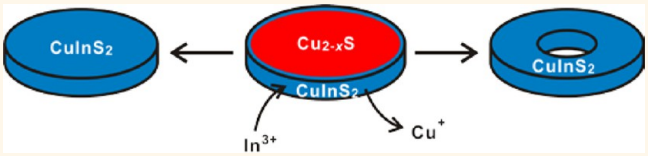

KEYWORDS: copper(I) indium disulfide · copper(I) sulfide · nanoplatelets · cation exchange · nanoscale Kirkendall Effect · hollow

We report herein that the morphologies of $CuInS_2$ nanocrystals prepared by ion exchange with $Cu_{2-x}S$ nanoplatelets (NPs) depend markedly on the indium precursor employed and the reaction temperature. More-ionic InX_3 precursors and/or higher exchange temperatures produce single-crystalline $CuInS_2$ NPs with preservation of the sizes and morphologies of the starting $Cu_{2-x}S$ NPs. More-covalent InX_3 precursors and/or lower exchange temperatures afford hollow-centered, ring-like nanocrystals as a result of the nanoscale Kirkendall Effect. The varying morphologies are attributed to the reaction barriers for In^{3+} insertion at the thin edges of the $Cu_{2-x}S$ NPs.

We are interested in pseudo-1D and pseudo-2D nanocrystals, such as nanowires,[1−3] nanobelts,[4,5] or nanosheets, for their potential to transport energy and charge without the requirement of interfacial hopping between nanocrystals.[6] Considerable interest has focused on $CuInS_2$ and related I−III−VI_2 nanostructures for applications in solar-energy conversion,[7−14] which attracted our attention to anisotropic nanocrystals of $CuInS_2$ and $CuInSe_2$.

The direct, solution-based syntheses of ternary and quaternary nanocrystals are complicated by the typically varying reactivities of the multiple precursors required.[15−18] In many cases, binary nanocrystals are first formed, which convert to the multinary target nanocrystals upon subsequent reaction, including by ion exchange.[18−21] Thus, a logical approach to the synthesis of anisotropic $CuInS_2$ and related nanocrystals is the initial preparation of binary nanocrystals to serve as the anisotropic template, followed by purposeful ion exchange to afford the desired ternary or multinary composition.[8]

Cu_2S and $Cu_{2-x}S$ readily undergo cation-exchange reactions.[22,23] Indeed, Donega and co-workers recently prepared $CuInS_2$ nanocrystals by partial indium-cation exchange into small $Cu_{2-x}S$ dot-like nanocrystals according to eq 1.[23] Lesnyak and co-workers reported similar observations at about the same time.[24] In these cases, cation exchange was aided by the small sizes and therefore short ion-diffusion distances within the pseudospherical nanocrystals. Lesnyak and co-workers also reported a

* Address correspondence to buhro@wustl.edu.

Received for review April 22, 2015 and accepted July 12, 2015.

Published online July 13, 2015
10.1021/acsnano.5b02427

related partial zinc and tin cation-exchange process with anisotropic $Cu_{2-x}S_ySe_{1-y}$ NPs.[25] However, the NP dimensions in that study were comparatively small (mean width = 18 nm; mean thickness = 4 nm). We show here that cation exchange into anisotropic template nanocrystals having longer diffusion distances is more complex. We determine how the eq 1 exchange process may be conducted using larger $Cu_{2-x}S$ NPs, with preservation of the initial platelet morphology.

$$2Cu_2S + In^{3+} \rightarrow CuInS_2 + 3Cu^{+} \quad (1)$$

We now report that the $CuInS_2$ nanocrystal morphologies obtained by cation exchange using $Cu_{2-x}S$ NPs having a mean width of 46 nm and a mean thickness of 13 nm depend on the In^{3+} source and the exchange temperature. Exchange reactions conducted with $InCl_3$ at 150 °C produce single-crystal hollow-centered nanoparticles, whereas those conducted with $InCl_3$ at 200 °C produce single-crystal NPs having the same mean dimensions as the initial template nanocrystals. Exchange reactions conducted with InI_3 at 150 °C produce nanorings with even larger center openings, whereas those conducted with $In(OAc)_3$ or $In(acac)_3$ at 150 °C produce NPs retaining the initial morphology. A mechanistic model is proposed to account for these experimental findings.

RESULTS

Preparation of $Cu_{2-x}S$ Template NPs. The starting $Cu_{2-x}S$ NPs were prepared by thermolysis of copper(I) dodecanethiolate ($CuSC_{12}H_{25}$) according to a procedure initially reported by Korgel and co-workers,[26,27] and later adapted by Tao and co-workers,[28−30] and Wu and co-workers.[31] We found that the thermolysis process was conveniently accelerated in the presence of *n*-dodecylamine, and so employed *n*-dodecylamine as an additive.

TEM images of the $Cu_{2-x}S$ NPs are provided in Figure 1. The nanocrystals exhibited the pseudohexagonal habit observed in the prior studies.[26−31] Statistical analysis of the images gave a mean NP (point-to-point) width of 46 ± 10 nm and a mean thickness of 13 ± 1 nm (Supporting Information Figure S1). The clean NP images and the platelet-wide Moiré fringes observed for some overlapping NPs suggested them to be single crystalline, as previously reported.[27] The $Cu_{2-x}S$ NPs exhibited the expected, broad localized surface plasmon resonance, centered near 1970 nm, in a visible-near-IR extinction spectrum (Supporting Information Figure S2).[29,30]

An XRD pattern of the $Cu_{2-x}S$ NPs is given in Figure 2. The Cu_2S-related phases exhibit structural polymorphism, with hexagonal high chalcocite (Cu_2S), monoclinic low chalcocite (Cu_2S), and monoclinic djurleite ($Cu_{2-x}S$, $x \approx 0.03-0.07$)[32] being among the most commonly observed polymorphs.[32] The pattern in

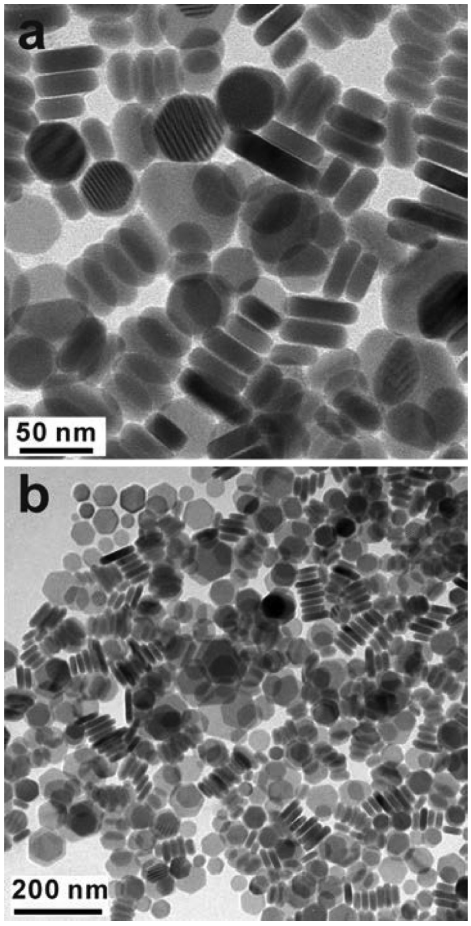

Figure 1. TEM images at two magnifications of the template $Cu_{2-x}S$ NPs prepared by adaptation of literature methods.[30]

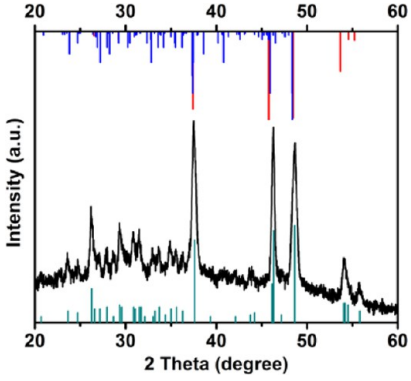

Figure 2. An XRD pattern of the $Cu_{2-x}S$ NPs (black), compared to the reference patterns of djurleite ($Cu_{2-x}S$, ICDD-PDF 00-023-0959, cyan), low chalcocite (Cu_2S, ICDD-PDF 00-033-0490, blue), and high chalcocite (Cu_2S, ICDD-PDF 00-026-1116, red).

Figure 2 corresponds most closely to djurleite, and clearly indicates a phase of lower symmetry than hexagonal high chalcocite. There is apparent disagreement in the literature concerning the structures of $Cu_{2-x}S$ NPs made by variations of the method employed here.[26−31] However, the structural differences between the phases are fairly small,[33] and both

djurleite and low chalcocite transform to high chalcocite above about 105 °C.[34] As the substitution reactions described here were conducted at temperatures above 105 °C, the structure of the $Cu_{2-x}S$ NPs under reaction conditions was presumed to be hexagonal high chalcocite.

Cation-Exchange Reactions Affording $CuInS_2$ Nanocrystals. An as-prepared *n*-dodecylamine dispersion of $Cu_{2-x}S$ NPs was heated to 150 °C, and a tri-*n*-octylphosphine (TOP) solution of $InCl_3$ (in the stoichiometric amount to prepare $CuInS_2$) was added. TOP was employed as the reaction solvent, in accord with Alivisatos and coworkers,[22] for its soft basicity and ability to complex the soft acid Cu^+. Reaction monitoring by XRD established that the ion-exchange process affording $CuInS_2$ was complete within 2 min. The XRD pattern of the resulting nanocrystals corresponded to $CuInS_2$ in the wurtzite structure (Figure 3). Thus, the hexagonal-close-packed anion sublattice of high chalcocite was retained, and the Cu and In ions adopted random positions within the cation sublattice, as is frequently observed in $CuInS_2$ nanocrystals.[13,23,24,35,36]

TEM images of these nanocrystals revealed that the NP morphology of the starting $Cu_{2-x}S$ nanocrystals was largely retained; however, most of them contained variously shaped holes through the large facets and near the platelet centers, sometimes with thinning or additional perforations elsewhere within the interiors of the nanocrystals (Figure 4). Edge views of the nanocrystals showed them to have irregularities in the thickness dimension, consistent with partial erosion of the initially dense $Cu_{2-x}S$ NPs. Analysis of mean NP composition by energy-dispersive X-ray spectroscopy (EDS) in the TEM gave the molar percentages 24.3% Cu, 24.1% In, and 51.6% S, close to the ideal phase composition (EDS data for all product specimens are listed in Supporting Information Table S2).

Figure 5a is a HRTEM image of a $CuInS_2$ nanocrystal in which the center was substantially eroded during

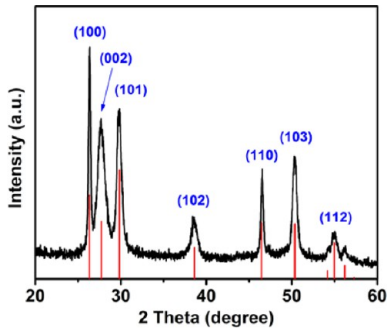

Figure 3. An XRD pattern of $CuInS_2$ nanocrystals resulting from ion exchange between $Cu_{2-x}S$ NPs and $InCl_3$ (150 °C, 2 min), compared to the reference pattern of $CuInS_2$ in the wurtzite structure (ICDD-PDF 01-077-9459). The crystalline coherence lengths in the lateral and thickness dimensions from the Scherrer equation were found to be 28 and 8.2 nm, respectively, using the 100, 002, and 110 reflections (see Supporting Information Table S1).

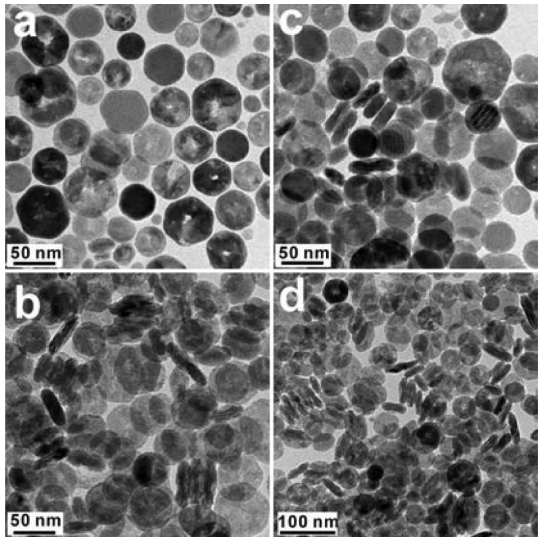

Figure 4. TEM images of $CuInS_2$ nanocrystals resulting from ion exchange between $Cu_{2-x}S$ NPs and $InCl_3$ (150 °C), revealing central holes and other thickness variations. All images were collected from the same synthetic sample.

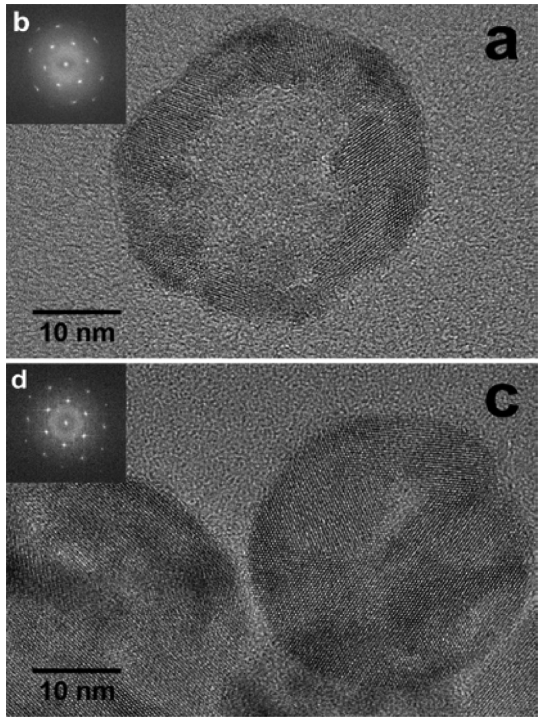

Figure 5. HRTEM images of $CuInS_2$ nanocrystals resulting from ion exchange between $Cu_{2-x}S$ NPs and $InCl_3$ (150 °C). The fast Fourier transforms in (b) and (d) correspond to the images in (a) and (c) (viewed in the wurtzite (001) zone axis), respectively. An enlargement of this figure is included as Supporting Information Figure S3, in which the lattice images are more clearly presented.

the exchange process, leaving an irregular, ring morphology. The fast Fourier transform (FFT) of this image (Figure 5b) exhibited nearly clean hexagonal symmetry, indicating the single-crystal character of the nanoring, and consistent with its wurtzite structure in the

[001] orientation. The $CuInS_2$ nanocrystal on the right of Figure 5c is more typical of the results at the 150 °C reaction temperature. An irregular hole slightly off center was apparent, and other thickness variations were evident. Even so, the FFT was consistent with a single crystal (Figure 5d). The results suggested that the $CuInS_2$ nanoring derived from a precursor single-crystal $Cu_{2-x}S$ NP, which, in the course of cation exchange, underwent a process that removed material from near the center of the NP.

The cation-exchange experiment was repeated with $Cu_{2-x}S$ NPs and $InCl_3$ as described above, except at a higher temperature of 180 °C. The product nanocrystals consisted of a high proportion of intact, fully dense $CuInS_2$ NPs, with the fewer eroded nanocrystals having comparatively smaller central holes (Supporting Information Figure S4). The TEM images in Figure 6 show the $CuInS_2$ nanocrystal morphologies from a cation-exchange experiment conducted at 200 °C. In this case, the product consisted almost entirely of intact $CuInS_2$ NPs. These NPs occasionally possessed surface blemishes consistent with erosion, but only rarely contained complete perforations through the NPs. Thus, the erosion process evident in Figures 4 and 5 was inhibited at higher cation-exchange temperatures.

To determine the possible role of the In^{3+}-precursor identity in the cation-exchange and erosion processes, cation exchange was conducted with $Cu_{2-x}S$ NPs and InI_3, as previously described and at the lower temperature of 150 °C. An XRD pattern collected after 2 min of reaction time established the cation exchange to $CuInS_2$ to be complete (Supporting Information Figure S5a). Figure 7 shows that the center-erosion process was enhanced with this precursor, resulting in nanorings having larger hollow centers in comparison to the cation exchange conducted with $InCl_3$. Close examination of several images like Figure 7a indicated that 61% of the NPs contained holes passing through the entire NP thickness, whereas 39% were thinned without complete perforations. The holes were distinguished by the clear observation of the holey-carbon-film background within them.

Statistical analysis of TEM images of the starting $Cu_{2-x}S$ NPs used in this synthesis gave mean widths of

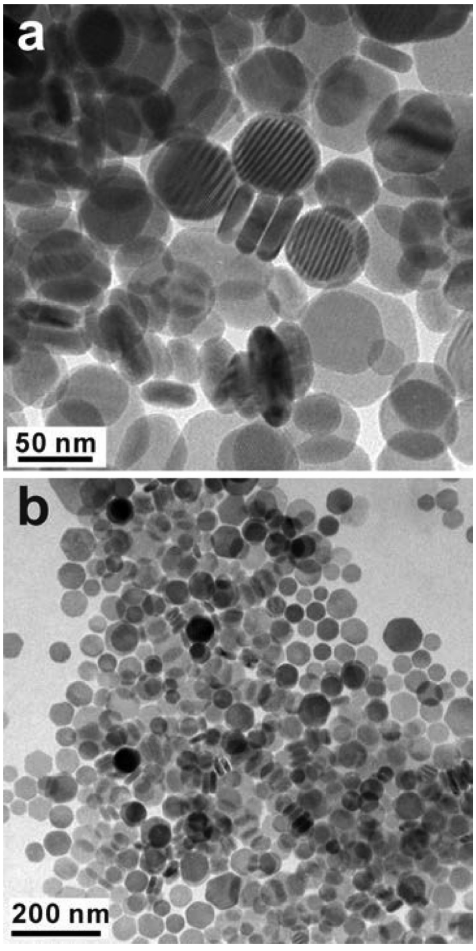

Figure 6. TEM images at two magnifications of $CuInS_2$ nanocrystals resulting from ion exchange between $Cu_{2-x}S$ NPs and $InCl_3$ (200 °C). The NPs are nearly free of central holes and other thickness variations.

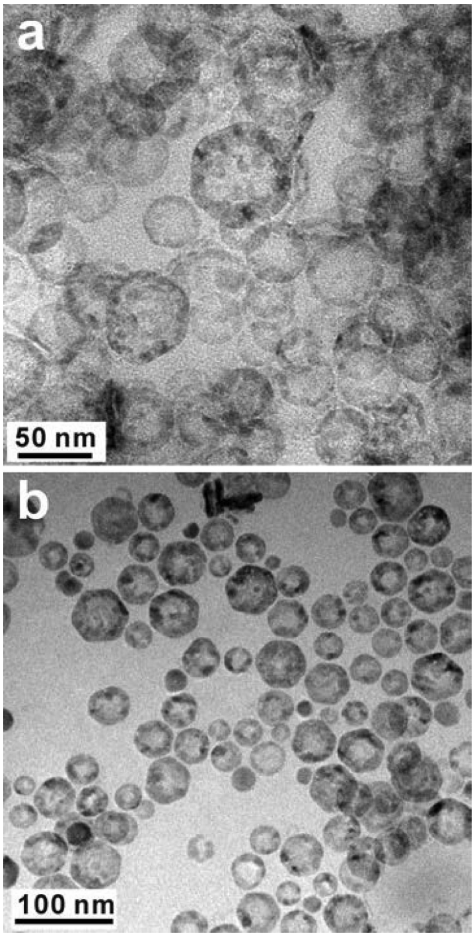

Figure 7. TEM images at two magnifications of $CuInS_2$ nanocrystals resulting from ion exchange between $Cu_{2-x}S$ NPs and InI_3 (150 °C), revealing large central holes and related thickness variations.

44 ± 9 nm. Similarly, the mean width of the resulting $CuInS_2$ nanorings and NPs was found to be 45 ± 9 nm, whereas the mean width of the central openings was 12 ± 11 nm. (To construct the mean central-opening width, those NPs with thinning but incomplete perforations were assigned a hole size of zero.) These results will be analyzed in the Discussion. EDS analysis established these nanorings and thinned NPs to be slightly S deficient (28.1% Cu, 29.0% In, and 42.9% S).

For comparison, cation exchange was also conducted with $Cu_{2-x}S$ NPs and $In(OAc)_3$ (in the stoichiometric amount to prepare $CuInS_2$) at 150 °C. XRD patterns collected after 2 and 4 min revealed mixtures of djurleite and (wurtzitic) $CuInS_2$, indicating incomplete ion exchange at those times. An XRD pattern collected after 10 min confirmed complete exchange to $CuInS_2$ (Supporting Information Figure S5b). The use of this In precursor resulted in fully dense, nearly blemish-free NPs, consistent with the elimination of the erosion process observed to some degree in most of the other cation-exchange reactions (Figure 8). Evidently, some characteristic of $In(OAc)_3$ allowed erosion-less exchange at the lowest reaction temperature investigated (150 °C), in contrast with the other precursors.

As stated above, the exchange process employing $In(OAc)_3$ at 150 °C gave intact $CuInS_2$ NPs, but required a longer reaction time to reach completion than the exchange reactions employing the In-halide precursors (10 min *vs* 2 min). To assist in elucidating the mechanism of the cation exchange, a related exchange reaction was conducted with $In(acac)_3$ (in the stoichiometric amount to prepare $CuInS_2$) at 150 °C. This process also afforded nearly fully intact, blemish-free $CuInS_2$ NPs (Figure 9). Reaction monitoring by XRD (Supporting Information Figure S5c) established this exchange process to be even slower, requiring 30 min to achieve complete exchange.

The relative slowness of the exchange processes with the $In(OAc)_3$ and $In(acac)_3$ precursors allowed NPs to be analyzed at an intermediate stage in the conversion of $Cu_{2-x}S$ to $CuInS_2$. Figure 10a,b shows HRTEM images of the faces and edges of the starting $Cu_{2-x}S$ NPs (an FFT of the face image is inset in Figure 10a). Figure 10e,f provides corresponding images of the fully exchanged

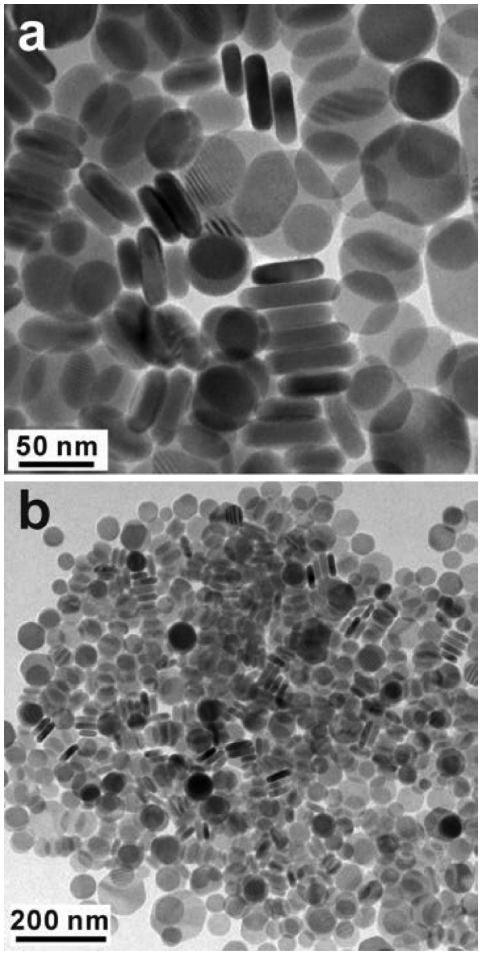

Figure 8. TEM images at two magnifications of $CuInS_2$ nanocrystals resulting from ion exchange between $Cu_{2-x}S$ NPs and $In(OAc)_3$ (150 °C). The NPs are free of central holes and other thickness variations.

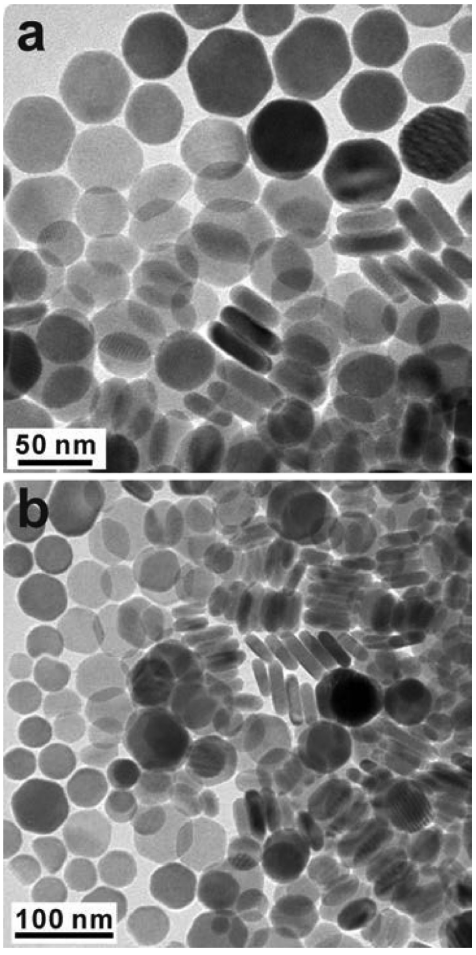

Figure 9. TEM images at two magnifications of $CuInS_2$ nanocrystals resulting from ion exchange between $Cu_{2-x}S$ NPs and $In(acac)_3$ (150 °C). The NPs are free of central holes and other thickness variations.

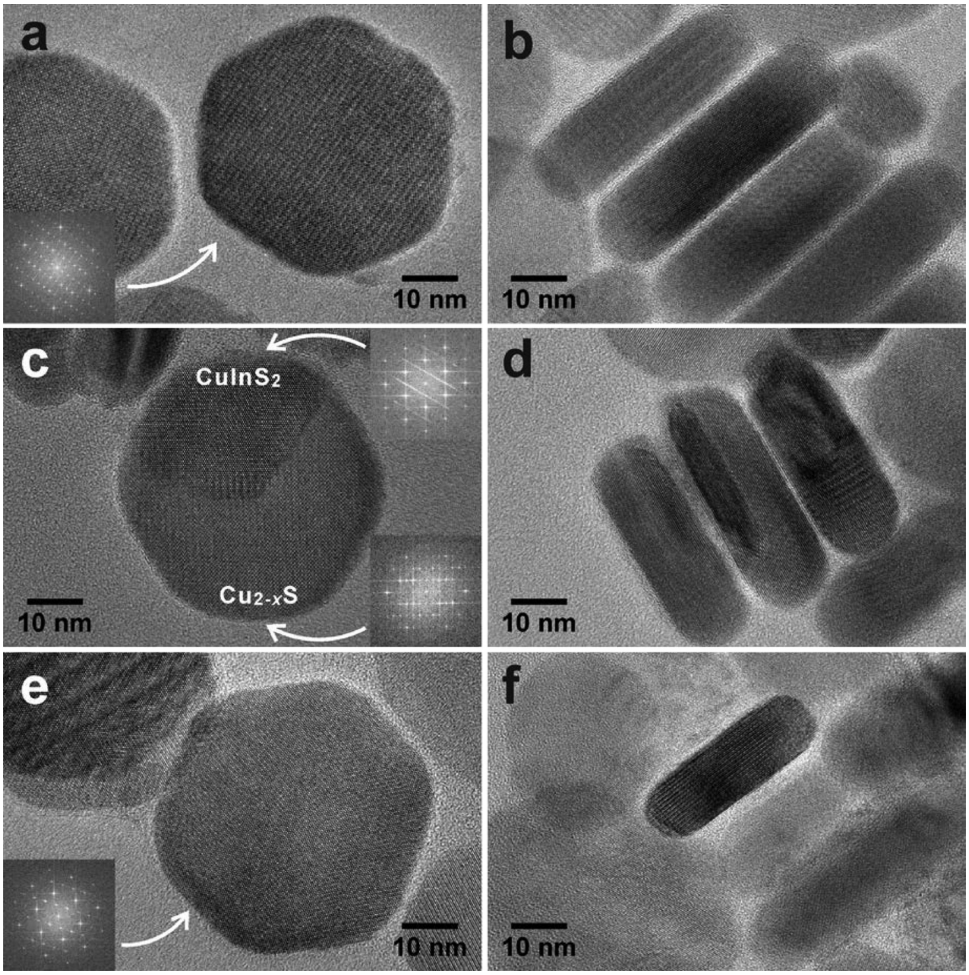

Figure 10. HRTEM images of NPs at different reaction stages during ion exchange between $Cu_{2-x}S$ NPs and $In(OAc)_3$ (150 °C). (a and b) Initial $Cu_{2-x}S$ NPs. (c and d) Partially exchanged NPs at an intermediate stage (2 min). (e and f) $CuInS_2$ NPs after complete ion exchange.

product $CuInS_2$ NPs, including an FFT inset. The images in Figure 10c,d were obtained after 2 min into the 10 min exchange process using the precursor $In(OAc)_3$.

Partial cation exchange was clearly evident in Figure 10c,d. Figure 10c contained a pie-like slice of $CuInS_2$ within a partially converted $Cu_{2-x}S$ NP. FFT images (inset) confirmed the structural assignments of these components. Figure 10d established that substitution process could also propagate in time throughout the thickness dimension of the NP. Most of the NPs examined in this specimen were found to be partially converted (a few were unreacted). Several additional HRTEM images of partially exchanged NPs are provided in Supporting Information Figure S6. These images are closely comparable to those reported by Manna and co-workers for partially cation-exchanged $Cu_{3-x}P$ NPs,[37] and consistent with cation exchange occurring through the NP edges (see below).

DISCUSSION

Nanoscale Kirkendall Effect. The operative process in forming the holey $CuInS_2$ NPs and hollow-centered $CuInS_2$ nanorings is the nanoscale Kirkendall Effect, first reported by Alivisatos and co-workers.[38] The Kirkendall Effect is a diffusion-related phenomenon occurring between reactive phases sharing an interface. If a phase A consists of spherical nanoparticles and a shell of phase B is deposited upon the phase-A nanoparticles, then the morphology of the resultant AB product nanoparticles may depend upon the relative diffusion rates of A and B through the AB product phase forming at the core−shell interface. In the initial Alivisatos study, Co nanoparticles were allowed to react with elemental S. The out-diffusion of Co was faster than the in-diffusion of S, resulting in hollowed Co_3S_4 nanoparticles, by the nanoscale Kirkendall Effect.

The nanoscale Kirkendall Effect is a general phenomenon.[39,40] This research field has recently been reviewed.[41] Significantly, the Effect has been shown to operate during ion-exchange processes, which is of particular relevance to the present study.[42]

Several studies have shown that ion-exchange reactions with NPs are initiated at the thin platelet edges rather than indiscriminately upon the broad top

and bottom facets.[37,43−46] For example, Manna and co-workers studied the conversion of $Cu_{3-x}P$ NPs to InP NPs by ion exchange with $InBr_3$.[37] Their results show clearly that InP first nucleates at the corners of the hexagonal $Cu_{3-x}P$ NPs, and that growth of the InP phase then propagates inward toward the centers of the NPs, until the entire NPs become transformed.

Cheon and co-workers have demonstrated that this basic mechanism is capable of converting NPs to nanotoroids or nanorings.[43−45] As shown in Figure 11, if ion-exchange occurs exclusively through the thin platelet edges, and if the out-diffusion of phase A is faster than the in-diffusion of B, then material is eroded from the center of the platelet and ultimately deposited near the edges, resulting in a ring or toroidal morphology. These morphologies form by the operation of the nanoscale Kirkendall Effect on NPs under the condition of exclusive edge diffusion.

An alternative pathway of indiscriminate ion exchange through the broad top and bottom facets, in which out-diffusion of A is faster than in-diffusion of B, would likely lead to the complete erosion of the NP, leaving no intact remnant behind. The top and bottom facets of NPs tend to be crystallographically flat, and well protected by self-assembled monolayers of ligand passivation, inhibiting ion exchange through those interfaces.[37] In contrast, thin NP edges generally tend to be ragged and defective, and less-well protected by ligation. Thus, ion exchange through the thin edges apparently has a lower barrier.

If cation exchange indeed occurs through the NP edges and with the operation of the nanoscale Kirkendall Effect, but without Ostwald ripening or material loss, then the product $CuInS_2$ NPs may reasonably be expected to have larger mean widths than the starting $Cu_{2-x}S$ NPs. We used the results of the InI_3 substitution, which produced the largest central holes, to assess this expectation. The mean width of the resulting $CuInS_2$ nanorings may be predicted by adding the mean volume of the central holes to the perimeter of the initial $Cu_{2-x}S$ NP mean dimensions.

We calculated the expected final widths by approximating the NPs and resulting nanorings as circular disks, using the mean NP and hole widths determined in the Results (see the Supporting Information). The final mean $CuInS_2$ NP width so approximated was 46 ± 12 nm, which is indistinguishable from the final mean width determined experimentally, 45 ± 9 nm. However, the final mean width determined experimentally was also indistinguishable from the mean width of the starting $Cu_{2-x}S$ NPs, 44 ± 9 nm. This analysis is complicated by the 39% of the product NPs lacking complete central holes. The expected mean NP width increase resulting from the operation of the nanoscale Kirkendall Effect is quite small, and our data are not able to show it.

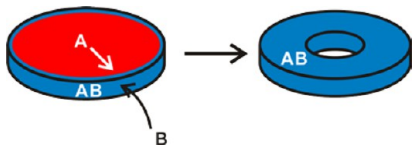

Figure 11. Schematic diagram depicting the operation of the Kirkendall Effect on NPs with out-diffusion of phase A and in-diffusion of phase B occurring only through the thin platelet edge.

Reaction Regimes for the Kirkendall Effect. Alivisatos and co-workers proposed four regimes for the reactions of phase-A particles with a phase B delivered to the particle surfaces by solution or gaseous deposition.[39] These regimes distinguish which reactions will result in solid AB particles with no hollowing, and which reactions will afford hollowed AB shells by the nanoscale Kirkendall Effect. Two of these reaction regimes are relevant to the results of the present study.

In the self-diffusion-limited regime,[39] the product nanostructure depends on the relative diffusion rates of A and B through the AB product phase. Hollowed particles form when the diffusion rate of A exceeds that of B. This scenario was presented above to introduce the nanoscale Kirkendall Effect. The high chalcocite phase of $Cu_{2-x}S$ exhibits high ionic conductivity associated with the high mobility of its constituent Cu^+ ions.[47] Thus, a more-rapid out-diffusion of Cu^+ and S^{2-} ions from phase A than in-diffusion of In^{3+} ions from phase B during ion exchange of the $Cu_{2-x}S$ NPs is readily imagined.

However, Cu^+ and S^{2-} should retain their diffusion-rate advantage at all temperatures studied, producing hollowed nanorings at all temperatures. Furthermore, the varying results obtained with the $InCl_3$, InI_3, $In(OAc)_3$, and $In(acac)_3$ precursors are not accounted for by the relative diffusion rates of Cu^+, S^{2-}, and In^{3+} ions within the NP crystal lattice, which should be the same, irrespective of precursor. Consequently, the ion-exchange processes investigated here do not appear to be operating within the self-diffusion-limited regime.

Another reaction regime identified by Alivisatos and co-workers is the collision-limited regime,[39] which we are adapting and renaming as the reaction-limited regime for the present discussion. The in-diffusion of In^{3+} into the $Cu_{2-x}S$ NPs is preceded by the adsorption of the InX_3 precursor on the NP edge facet (Figure 12). The X^- ligands from the precursor must be displaced to allow entry of the In^{3+} into the crystal lattice. Figure 12 suggests that such displacement occurs by nucleophilic attack of lattice S^{2-} ions on the adsorbed InX_3 precursor.

Consequently, a reaction barrier or barriers must be overcome in this nucleophilic displacement process to insert In^{3+} ions into the $Cu_{2-x}S$ NPs. We propose the height of the reaction barrier to be determined by the leaving-group ability of the X^- ligands, in the sequence $I^- < Cl^- < {}^-OAc \approx CH_3C(O)CH_2C(CH_3)O^-$ ($acac^-$).[48]

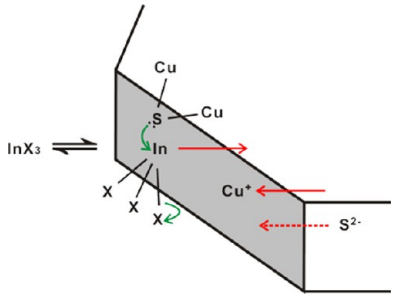

Figure 12. Schematic diagram depicting the edge adsorption of the InX_3 precursor, the nucleophilic displacement of X^- by a lattice S^{2-} ion, the in-diffusion of In^{3+}, and the out-diffusion of Cu^+ and S^{2-}.

Thus, the X^- displacement barriers scale with the ionicity of the InX_3 precursor, with the highest reaction barriers for InI_3, and the lowest for $In(OAc)_3$ and $In(acac)_3$.

High reaction barriers for In^{3+} entry at the NP edges decreases the effective rate of In^{3+} incorporation, and thus limits the availability of In^{3+} for in-diffusion, allowing the out-diffusion of $Cu_{2-x}S$ to outcompete the in-diffusion of In^{3+}. Hollow-centered $CuInS_2$ nanorings form under these conditions. In contrast, low reaction barriers for In^{3+} entry at the NP edges provide a higher rate of lattice In^{3+} incorporation, supporting balanced stoichiometries of In^{3+} in-diffusion and Cu^+ out-diffusion, given that the ion-exchange process is not diffusion limited (see above).

In the reaction-limited regime with low barriers for In^{3+} incorporation, ion exchange occurs to leave the fully dense NP morphology intact. The lower reaction barriers may be obtained either at higher temperature (as in for $InCl_3$), or with a better X^- leaving group (^-OAc or $acac^-$). Thus, the InX_3 precursor and reaction temperature determine the presence or absence of the nanoscale Kirkendall Effect and, therefore, the final nanocrystal morphology resulting from the ion exchange. The Kirkendall Effect operates in the reaction-limited regime when the barriers for ion incorporation are high.

We note that the longer reaction times (10 and 30 min, respectively) required for ion exchange using $In(OAc)_3$ and $In(acac)_3$ than for $InCl_3$ or InI_3 (<2 min) may seem in contradiction of the faster lattice incorporation of In^{3+} from $In(OAc)_3$ and $In(acac)_3$. However, adsorption of the InX_3 precursor onto the NP edge facet must precede In^{3+} incorporation, and we surmise that the adsorption pre-equilibrium lies further to the left in Figure 12 for the sterically encumbered $In(OAc)_3$ and $In(acac)_3$ precursors relative to the sterically smaller $InCl_3$ or InI_3 precursors. Because the acac ligand is larger than OAc, and because $In(acac)_3$ has a sterically saturated, 6-coordinate, pseudo-octahedral structure,[49] its adsorption pre-equilibrium lies even further leftward than that of $In(OAc)_3$, and consequently, the overall exchange kinetics are the slowest for $In(acac)_3$. We further note that no driving force exists for the nanoscale Kirkendall Effect *until* the InX_3 precursor is actually adsorbed onto the $Cu_{2-x}S$ NP. Thus, we propose that the slower overall exchange kinetics for $In(OAc)_3$ and $In(acac)_3$ reflect slower effective adsorption kinetics due to the position of the adsorption pre-equilibrium.

The tendency of the nanoscale Kirkendall Effect to accompany ion-exchange processes in nanocrystals appears to be greater for nanocrystals having larger size dimensions. Thus, there is no hint of the Effect in small (2−8 nm), pseudospherical $Cu_{2-x}S$ nanocrystals undergoing ion exchange with In^{3+}.[23,24] Nor is hollowing or hole formation observed upon ion exchange in smaller $Cu_{2-x}S$ NPs having widths of 18 nm.[25] Interestingly, however, Hillhouse and co-workers published[50] strikingly beautiful hexagonal nanorings of $CuInSe_2$ having widths of 30−35 nm (see Figure 3 in ref 50). We surmise that these nanocrystals resulted from In^{3+} ion exchange into initially formed $Cu_{2-x}Se$ NPs, under the operation of the nanoscale Kirkendall Effect. The Kirkendall Effect is exacerbated in nanocrystals of larger dimension because of the lower *effective* rates of ion in-diffusion over the longer diffusion distances.

CONCLUSION

Ion exchange provides a means of preparing nanocrystals of complex ternary or quaternary phases from binary template nanocrystals. However, the nanoscale Kirkendall Effect must remain inactive to preserve the original morphology of the template nanocrystals. The use of molecular precursors to provide the exchange ions may cause the exchange process to occur in the reaction-limited regime, resulting in low relative rates of incorporation of the exchange ion, which triggers the nanoscale Kirkendall Effect and the consequent hollowing of the product nanocrystals. This effect is deactivated by the use of higher reaction temperatures, precursors of higher ionicity, or template nanocrystals of smaller dimension.

EXPERIMENTAL SECTION

Materials and General Procedures. *n*-Dodecylamine (98%), tri-*n*-octylphosphine (TOP) (97%), $In(OAc)_3$ (99.99%, metal basis), and $In(acac)_3$ (99.99%+) were obtained from Sigma-Aldrich. $InCl_3$ (anhydrous, 99.999%-In) and InI_3 (99.999%-In) were obtained from Strem Chemicals. All were used as received and stored under N_2. Toluene (CHROMASOLV for HPLC, 99.9%) from Sigma-Aldrich, methanol (≥99.8%) from Sigma-Aldrich, carbon tetrachloride (CHROMASOLV for HPLC, ≥99.9%), *n*-dodecanethiol (98%) from Sigma-Aldrich, $Cu(NO_3)_2 \cdot 3H_2O$ (99.5%) from Strem Chemicals, and ethyl alcohol (100%) from Pharmco-Aaper were used as received and stored under ambient conditions. Copper(I) dodecanethiolate ($CuSC_{12}H_{25}$) was prepared following a literature method[30] and stored under dry N_2.

Transmission electron microscopy (TEM) sample grids (Ni with holey carbon film) were obtained from Ted Pella, Inc. X-ray Diffraction (XRD) sample holders (zero-diffraction silicon plate, 24.6 mm diameter and 1.0 mm thickness, with cavity 10 mm diameter and 0.2 mm depth) were obtained from the MTI Corporation.

All synthetic procedures were conducted under dry N_2, except for the final purification steps, which were conducted in the ambient atmosphere.

Characterization Methods. Low-resolution TEM images and EDS analysis data were collected using a JEOL 2000FX TEM operating at 200 kV. High-resolution TEM images were collected using a JEOL JEM-2100F field emission (FE)—scanning transmission electron microscope. Both low- and high-resolution TEM samples were prepared by dipping TEM grids into a toluene dispersion (5—6 mL) of a purified specimen, and immediately removed to allow evaporation of the solvent. XRD patterns were collected and processed using a Bruker d8 Advance X-ray Diffractometer with Cu Kα radiation (λ = 1.541845 Å) and the Bruker Diffrac.Eva program. The XRD samples were prepared from toluene dispersions (0.5 mL) of purified specimens. The concentrated suspension was drop-casted onto a silicon sample holder, and dried in the fume hood. UV—visible, near-infrared spectra were collected using a Perkin Lambda 950 UV/vis spectrometer. Spectral data were obtained from CCl_4 dispersions of purified $Cu_{2-x}S$ nanoplatelets, and toluene dispersions of as-made $CuInS_2$ nanocrystals, in quartz cuvettes.

Synthesis of Copper(I) Sulfide Nanoplatelets ($Cu_{2-x}S$ NPs). $Cu_{2-x}S$ NPs were synthesized by adapting a literature method.[30] In a typical procedure, $CuSC_{12}H_{25}$ (0.026 g, 0.10 mmol) and *n*-dodecylamine (0.370 g, 2.00 mmol) were combined in a Schlenk tube, and heated in a 200 °C salt bath ($NaNO_3$/KNO_3/$Ca(NO_3)_2$, 21%:54%:25% by mol) for 8 h. The $CuSC_{12}H_{25}$ dissolved in melting *n*-dodecylamine rapidly upon heating, forming a light yellow solution. The reaction mixture turned brown within 20 min, and darker with extended reaction time, finally forming a dark brown-black suspension after 8 h.

The mixture was allowed to cool to room temperature under N_2. The as-made product mixture was used for cation exchange. For characterization, $Cu_{2-x}S$ NPs were isolated by adding toluene and methanol (6 mL total, volume ratio 2:1), followed by centrifuging for 5 min at 1500 rpm and discarding the supernatant. This purification procedure was repeated twice, before the $Cu_{2-x}S$ NPs were redispersed in toluene for TEM and XRD characterization, and in CCl_4 for visible-near-IR spectroscopy.

Synthesis of Copper(I) Indium Sulfide Nanoplatelets ($CuInS_2$ NPs) by Cation Exchange. In a typical procedure, $InCl_3$ (0.006 g, 0.03 mmol) was added to TOP (2 g), which dissolved after sonication for 10 min at room temperature. The as-made $Cu_{2-x}S$ NPs product mixture in a Schlenk tube was heated in salt bath (at 150, 180, or 200 °C) forming a black suspension, and into which the $InCl_3$ solution was swiftly injected *via* syringe. The Schlenk tube was held at a constant temperature (150, 180, or 200 °C) for 2 h, and aliquots were removed for analysis during the reaction.

$CuInS_2$ NPs were isolated by adding toluene and methanol (6 mL total, volume ratio 2:1), followed by centrifuging for 5 min at 1500 rpm and discarding the supernatant. This purification procedure was repeated twice, and then the $CuInS_2$ NPs were redispersed in toluene for TEM and XRD characterization. The as-made $CuInS_2$ NPs were dispersed in toluene for UV—visible spectroscopy.

The same general procedure was employed with InI_3, $In(OAc)_3$, or $In(acac)_3$ as the indium precursor, except for the initial dissolution step. The precursor InI_3 (0.013 g, 0.03 mmol) was dissolved in TOP after sonication for 5 min at room temperature. The precursor $In(OAc)_3$ (0.008 g, 0.03 mmol) was dispersed in TOP after sonication for 30 min at room temperature; in some procedures, *n*-dodecylamine (0.051 g, 0.3 mmol) was added and the mixture was warmed to 150 °C (10 min) to aid in dissolution. The precursor $In(acac)_3$ (0.011 g, 0.03 mmol) was dispersed in TOP after sonication for 20 min at room temperature, and the mixture was warmed to 150 °C (10 min) to aid in dissolution.

Conflict of Interest: The authors declare no competing financial interest.

Acknowledgment. This work was supported by the NSF under grant CHE-1306507.

Supporting Information Available: Visible-near-IR spectrum of $Cu_{2-x}S$ NPs, UV—vis spectra of $CuInS_2$ nanocrystals, $Cu_{2-x}S$ NP and $CuInS_2$ nanocrystals size distributions, composition analysis of $CuInS_2$ nanocrystals, additional XRD patterns, additional TEM images and calculation of NP width change before and after ion exchange. The Supporting Information is available free of charge on the ACS Publications website at DOI: 10.1021/acsnano.5b02427.

REFERENCES AND NOTES

1. Glennon, J. J.; Tang, R.; Buhro, W. E.; Loomis, R. A. Synchronous Photoluminescence Intermittency (Blinking) along Whole Semiconductor Quantum Wires. *Nano Lett.* **2007**, *7*, 3290–3295.
2. Wayman, V. L.; Morrison, P. J.; Wang, F.; Tang, R.; Buhro, W. E.; Loomis, R. A. Bound 1D Excitons in Single CdSe Quantum Wires. *J. Phys. Chem. Lett.* **2012**, *3*, 2627–2632.
3. Liu, Y.-H.; Wang, F.; Hoy, J.; Wayman, V. L.; Steinberg, L. K.; Loomis, R. A.; Buhro, W. E. Bright Core—Shell Semiconductor Quantum Wires. *J. Am. Chem. Soc.* **2012**, *134*, 18797–18803.
4. Liu, Y.-H.; Wang, F.; Wang, Y.; Gibbons, P. C.; Buhro, W. E. Lamellar Assembly of Cadmium Selenide Nanoclusters into Quantum Belts. *J. Am. Chem. Soc.* **2011**, *133*, 17005–17013.
5. Liu, Y.-H.; Wayman, V. L.; Gibbons, P. C.; Loomis, R. A.; Buhro, W. E. Origin of High Photoluminescence Efficiencies in CdSe Quantum Belts. *Nano Lett.* **2010**, *10*, 352–357.
6. Wang, F.; Wang, Y.; Liu, Y.-H.; Morrison, P. J.; Loomis, R. A.; Buhro, W. E. Two-Dimensional Semiconductor Nanocrystals: Properties, Templated Formation, and Magic-Size Nanocluster Intermediates. *Acc. Chem. Res.* **2015**, *48*, 13–21.
7. Wooten, A. J.; Werder, D. J.; Williams, D. J.; Casson, J. L.; Hollingsworth, J. A. Solution—Liquid—Solid Growth of Ternary Cu—In—Se Semiconductor Nanowires from Multiple- and Single-Source Precursors. *J. Am. Chem. Soc.* **2009**, *131*, 16177–16188.
8. Xu, J.; Lee, C.-S.; Tang, Y.-B.; Chen, X.; Chen, Z.-H.; Zhang, W.-J.; Lee, S.-T.; Zhang, W.; Yang, Z. Large-Scale Synthesis and Phase Transformation of CuSe, $CuInSe_2$, and $CuInSe_2$/$CuInS_2$ Core/Shell Nanowire Bundles. *ACS Nano* **2010**, *4*, 1845–1850.
9. Li, Q.; Zou, C.; Zhai, L.; Zhang, L.; Yang, Y.; Chen, X.; Huang, S. Synthesis of Wurtzite $CuInS_2$ Nanowires by Ag_2S-Catalyzed Growth. *CrystEngComm* **2013**, *15*, 1806–1813.
10. Choi, Y.; Beak, M.; Yong, K. Solar-Driven Hydrogen Evolution Using a $CuInS_2$/CdS/ZnO Heterostructure Nanowire Array as an Efficient Photoanode. *Nanoscale* **2014**, *6*, 8914–8918.
11. Wu, X.-J.; Huang, X.; Qi, X.; Li, H.; Li, B.; Zhang, H. Copper-Based Ternary and Quaternary Semiconductor Nanoplates: Templated Synthesis, Characterization, and Photoelectrochemical Properties. *Angew. Chem., Int. Ed.* **2014**, *53*, 8929–8933.
12. Li, Q.; Zhai, L.; Zou, C.; Huang, X.; Zhang, L.; Yang, Y.; Chen, X.; Huang, S. Wurtzite $CuInS_2$ and $CuIn_xGa_{1-x}S_2$ Nanoribbons: Synthesis, Optical and Photoelectrical Properties. *Nanoscale* **2013**, *5*, 1638–1648.
13. Qi, Y.; Liu, Q.; Tang, K.; Liang, Z.; Ren, Z.; Liu, X. Synthesis and Characterization of Nanostructured Wurtzite $CuInS_2$: A New Cation Disordered Polymorph of $CuInS_2$. *J. Phys. Chem. C* **2009**, *113*, 3939–3944.
14. Sheng, X.; Wang, L.; Luo, Y.; Yang, D. Synthesis of Hexagonal Structured Wurtzite and Chalcopyrite $CuInS_2$ *via* a Simple Solution Route. *Nanoscale Res. Lett.* **2011**, *6*, 562.
15. Liu, X.; Wang, X.; Swihart, M. T. Composition-Dependent Crystal Phase, Optical Properties, and Self-Assembly of Cu—Sn—S Colloidal Nanocrystals. *Chem. Mater.* **2015**, *27*, 1342–1348.

16. Koo, B.; Patel, R. N.; Korgel, B. A. Wurtzite−Chalcopyrite Polytypism in $CuInS_2$ Nanodisks. *Chem. Mater.* **2009**, *21*, 1962–1966.
17. Choi, S.-H.; Kim, E.-G.; Hyeon, T. One-Pot Synthesis of Copper−Indium Sulfide Nanocrystal Heterostructures with Acorn, Bottle, and Larva Shapes. *J. Am. Chem. Soc.* **2006**, *128*, 2520–2521.
18. Connor, S. T.; Hsu, C.-M.; Weil, B. D.; Aloni, S.; Cui, Y. Phase Transformation of Biphasic Cu_2S−$CuInS_2$ to Monophasic $CuInS_2$ Nanorods. *J. Am. Chem. Soc.* **2009**, *131*, 4962–4966.
19. Tan, J. M. R.; Lee, Y. H.; Pedireddy, S.; Baikie, T.; Ling, X. Y.; Wong, L. H. Understanding the Synthetic Pathway of a Single-Phase Quarternary Semiconductor Using Surface-Enhanced Raman Scattering: A Case of Wurtzite Cu_2ZnSnS_4 Nanoparticles. *J. Am. Chem. Soc.* **2014**, *136*, 6684–6692.
20. Ahmadi, M.; Pramana, S. S.; Xi, L.; Boothroyd, C.; Lam, Y. M.; Mhaisalkar, S. Evolution Pathway of CIGSe Nanocrystals for Solar Cell Applications. *J. Phys. Chem. C* **2012**, *116*, 8202–8209.
21. Collord, A. D.; Hillhouse, H. W. Composition Control and Formation Pathway of CZTS and CZTGS Nanocrystal Inks for Kesterite Solar Cells. *Chem. Mater.* **2015**, *27*, 1855–1862.
22. Luther, J. M.; Zheng, H.; Sadtler, B.; Alivisatos, A. P. Synthesis of PbS Nanorods and Other Ionic Nanocrystals of Complex Morphology by Sequential Cation Exchange Reactions. *J. Am. Chem. Soc.* **2009**, *131*, 16851–16857.
23. van der Stam, W.; Berends, A. C.; Rabouw, F. T.; Willhammar, T.; Ke, X.; Meeldijk, J. D.; Bals, S.; de Mello Donega, C. Luminescent $CuInS_2$ Quantum Dots by Partial Cation Exchange in $Cu_{2-x}S$ Nanocrystals. *Chem. Mater.* **2015**, *27*, 621–628.
24. Akkerman, Q. A.; Genovese, A.; George, C.; Prato, M.; Moreels, I.; Casu, A.; Marras, S.; Curcio, A.; Scarpellini, A.; Pellegrino, T.; et al. From Binary Cu_2S to Ternary Cu−In−S and Quaternary Cu−In−Zn−S Nanocrystals with Tunable Composition *via* Partial Cation Exchange. *ACS Nano* **2015**, *9*, 521–531.
25. Lesnyak, V.; George, C.; Genovese, A.; Prato, M.; Casu, A.; Ayyappan, S.; Scarpellini, A.; Manna, L. Alloyed Copper Chalcogenide Nanoplatelets *via* Partial Cation Exchange Reactions. *ACS Nano* **2014**, *8*, 8407–8418.
26. Larsen, T. H.; Sigman, M.; Ghezelbash, A.; Doty, R. C.; Korgel, B. A. Solventless Synthesis of Copper Sulfide Nanorods by Thermolysis of a Single Source Thiolate-Derived Precursor. *J. Am. Chem. Soc.* **2003**, *125*, 5638–5639.
27. Sigman, M. B.; Ghezelbash, A.; Hanrath, T.; Saunders, A. E.; Lee, F.; Korgel, B. A. Solventless Synthesis of Monodisperse Cu_2S Nanorods, Nanodisks, and Nanoplatelets. *J. Am. Chem. Soc.* **2003**, *125*, 16050–16057.
28. Bryks, W.; Wette, M.; Velez, N.; Hsu, S.-W.; Tao, A. R. Supramolecular Precursors for the Synthesis of Anisotropic Cu_2S Nanocrystals. *J. Am. Chem. Soc.* **2014**, *136*, 6175–6178.
29. Hsu, S.-W.; Bryks, W.; Tao, A. R. Effects of Carrier Density and Shape on the Localized Surface Plasmon Resonances of $Cu_{2-x}S$ Nanodisks. *Chem. Mater.* **2012**, *24*, 3765–3771.
30. Hsu, S.-W.; On, K.; Tao, A. R. Localized Surface Plasmon Resonances of Anisotropic Semiconductor Nanocrystals. *J. Am. Chem. Soc.* **2011**, *133*, 19072–19075.
31. Chen, Y.-B.; Chen, L.; Wu, L.-M. The Structure-Controlling Solventless Synthesis and Optical Properties of Uniform Cu_2S Nanodisks. *Chem. - Eur. J.* **2008**, *14*, 11069–11075.
32. Potter, R. W. An Electrochemical Investigation of the System Copper-Sulfur. *Econ. Geol. Bull. Soc. Econ. Geol.* **1977**, *72*, 1524–1542.
33. Evans, H. T., Jr. Djurleite ($Cu_{1.94}S$) and Low Chalcocite (Cu_2S): New Crystal Structure Studies. *Science* **1979**, *203*, 356–358.
34. Buerger, M. J.; Wuensch, B. J. Distribution of Atoms in High Chalcocite, Cu_2S. *Science* **1963**, *141*, 276–277.
35. Pan, D.; An, L.; Sun, Z.; Hou, W.; Yang, Y.; Yang, Z.; Lu, Y. Synthesis of Cu−In−S Ternary Nanocrystals with Tunable Structure and Composition. *J. Am. Chem. Soc.* **2008**, *130*, 5620–5621.
36. Lu, X.; Zhuang, Z.; Peng, Q.; Li, Y. Controlled Synthesis of Wurtzite $CuInS_2$ Nanocrystals and Their Side-By-Side Nanorod Assemblies. *CrystEngComm* **2011**, *13*, 4039–4045.
37. De Trizio, L.; Gaspari, R.; Bertoni, G.; Kriegel, I.; Moretti, L.; Scotognella, F.; Maserati, L.; Zhang, Y.; Messina, G. C.; Prato, M.; et al. $Cu_{3-x}P$ Nanocrystals as a Material Platform for Near-Infrared Plasmonics and Cation Exchange Reactions. *Chem. Mater.* **2015**, *27*, 1120–1128.
38. Yin, Y.; Rioux, R. M.; Erdonmez, C. K.; Hughes, S.; Somorjai, G. A.; Alivisatos, A. P. Formation of Hollow Nanocrystals Through the Nanoscale Kirkendall Effect. *Science* **2004**, *304*, 711–714.
39. Cabot, A.; Ibáñez, M.; Guardia, P.; Alivisatos, A. P. Reaction Regimes on the Synthesis of Hollow Particles by the Kirkendall Effect. *J. Am. Chem. Soc.* **2009**, *131*, 11326–11328.
40. Niu, K.-Y.; Park, J.; Zheng, H.; Alivisatos, A. P. Revealing Bismuth Oxide Hollow Nanoparticle Formation by the Kirkendall Effect. *Nano Lett.* **2013**, *13*, 5715–5719.
41. Wang, W.; Dahl, M.; Yin, Y. Hollow Nanocrystals through the Nanoscale Kirkendall Effect. *Chem. Mater.* **2013**, *25*, 1179–1189.
42. Liang, X.; Wang, X.; Zhuang, Y.; Xu, B.; Kuang, S.; Li, Y. Formation of CeO_2−ZrO_2 Solid Solution Nanocages with Controllable Structures *via* Kirkendall Effect. *J. Am. Chem. Soc.* **2008**, *130*, 2736–2737.
43. Jeong, S.; Han, J. H.; Jang, J.-t.; Seo, J.-w.; Kim, J.-G.; Cheon, J. Transformative Two-Dimensional Layered Nanocrystals. *J. Am. Chem. Soc.* **2011**, *133*, 14500–14503.
44. Han, J. H.; Lee, S.; Yoo, D.; Lee, J.-H.; Jeong, S.; Kim, J.-G.; Cheon, J. Unveiling Chemical Reactivity and Structural Transformation of Two-Dimensional Layered Nanocrystals. *J. Am. Chem. Soc.* **2013**, *135*, 3736–3739.
45. Han, J. H.; Lee, S.; Cheon, J. Synthesis and Structural Transformations of Colloidal 2D Layered Metal Chalcogenide Nanocrystals. *Chem. Soc. Rev.* **2013**, *42*, 2581–2591.
46. Sines, I. T.; Vaughn, D. D.; Biacchi, A. J.; Kingsley, C. E.; Popczun, E. J.; Schaak, R. E. Engineering Porosity into Single-Crystal Colloidal Nanosheets Using Epitaxial Nucleation and Chalcogenide Anion Exchange Reactions: The Conversion of SnSe to SnTe. *Chem. Mater.* **2012**, *24*, 3088–3093.
47. Hirahara, E. The Electrical Conductivity and Isothermal Hall Effect in Cuprous Sulfide, Semi-Conductor. *J. Phys. Soc. Jpn.* **1951**, *6*, 428–437.
48. Lowry, T. H.; Richardson, K. S. *Mechanism and Theory in Organic Chemistry*; Harper & Row: New York, 1976; pp 192−194.
49. Palenik, G. J.; Dymock, K. R. The Structure of Tris(2,4-pentanedionato)indium(III). *Acta Crystallogr., Sect. B: Struct. Crystallogr. Cryst. Chem.* **1980**, *36*, 2059–2063.
50. Guo, Q.; Kim, S. J.; Kar, M.; Shafarman, W. N.; Birkmire, R. W.; Stach, E. A.; Agrawal, R.; Hillhouse, H. W. Development of $CuInSe_2$ Nanocrystal and Nanoring Inks for Low-Cost Solar Cells. *Nano Lett.* **2008**, *8*, 2982–2987.